Insights into the regulation of the human Cop9 signalosome catalytic subunit, CSN5/Jab1

Aude Echalier[1§], Yunbao Pan[2*], Melissa Birol[1*], Nicolas Tavernier[5], Lionel Pintard[5], François Hoh[1], Christine Ebel[4], Nathalie Galophe[1], François X. Claret[2,3], Christian Dumas[1]

[1]Centre de Biochimie Structurale, Centre National de la Recherche Scientifique (CNRS) UMR 5048 - UM1 - INSERM UMR 1054, Montpellier, France
[2]Department of Systems Biology, The University of Texas MD Anderson Cancer Center, Houston, TX 77030 USA
[3]Cancer Biology Program (CBS) and Experimental Therapeutic Program, The University of Texas Graduate School of Biomedical Sciences at Houston, Houston, TX 77030 USA
[4]CEA - CNRS - Université Joseph Fourier Grenoble 1, Institut de Biologie Structurale Jean-Pierre Ebel, Grenoble, France
[5]Institut Jacques Monod, Paris, France
* these authors contributed equally to this work.

§ to whom the correspondence may be address: Aude Echalier, Centre de Biochimie Structurale, 29 rue de Navacelles, 34090 Montpellier cedex. Phone: +33 - (0) 4 67 41 77 08; Fax: +33 - (0) 4 67 41 79 13; Email: aude.echalier-glazer@cbs.cnrs.fr.

Supplementary results

Overall structure and oligomeric arrangement

The characteristics of each plausible oligomeric arrangement identified in the crystal were evaluated by PISA (1) (Table S2), which highlights two types of dimers (A-B and A-A') and a D2 tetramer that bury a total surface area of 2,112, 1,950 and 8,970 $Å^2$, respectively (Fig. S1A,S2). Several lines of evidences in the literature suggest the propensity of CSN5 to form oligomers. Indeed, non-denaturing MS and proteomic evaluations revealed the presence of oligomers *in vitro* (2, 3). In eukaryotic cells, CSN5 is present in not only the CSN complex, but also in smaller complexes (between 70 and 150 kDa, while the monomer is 29 kDa) that might correspond to CSN5 oligomeric forms (4-7). Together with these evidences described in the literature but not further experimentally probed, the crystal dimer properties led us to explore the functional relevance of CSN5 oligomerisation, both *in vitro* and *in vivo*.

Evaluation of the dimer disruption extent was carried out *in vitro* by DLS and AUC and *in vivo* by co-immunoprecipitation. Two leucine residues (Leu237 and Leu240) placed on one side of the helix α4, facing α6, as well as the Arg129 residue were consequently selected (Fig. S1E). DLS measurements on these interfacial mutants clearly showed a drop in particle diameter as compared to those on the WT protein (Table S3). This drop, particularly marked between WT and the double mutant L237Q/L240K, is compatible with the transition from A-B dimer to mostly monomeric species. In contrast, the deletion of the C-terminal tail that mediates the A-A' dimer does not affect as much the assembly, further supporting the idea that the A-B dimer is the preponderant assembly in solution. AUC experiments confirmed that the L237Q/L240K variant of CSN5 is mostly monomeric (Fig. S1E; Table S4). Similar results were obtained in *in vivo* experiments, where the single Arg129A or the double L237Q/L240K mutations significantly reduced dimer formation (70-80% inhibition), thus confirming that the A-B dimer is the predominant one *in vivo* (Fig. S1G).

The MPN domain. The core of the MPN fold that consists of the central β-sheet and three α-helices (residues 51–224) is largely conserved in the MPN domain-containing structures solved to date, with a mean r.m.s. deviation of 3.2 Å over an average of 124 residues (as calculated by the DALI server (8)) and a mean r.m.s. deviation of 1 Å for the 54 most central residues (as calculated by Chimera (9)), including the recently reported CSN6 structure from Drosophila (10).

Supplementary material and methods.

Construct design, cloning, expression and purification.

cDNA coding for full-length (1-334) CSN5 was cloned into the pGEX-6P1 vector (GE Healthcare). Expression trials under standard conditions revealed that the majority of recombinant CSN5 in *E. coli* was expressed in truncated forms ranging from 29 to 31 kDa. The corresponding purified CSN5 fragments were identified using N-terminal sequencing (carried out by Dr. L. Coquet, Université de Rouen) and electrospray–mass spectrometry (kindly carried out by Dr. D. Staunton, University of Oxford). The lowest-molecular-weight fragment was assigned the sequence 1-257. Subcloning of the corresponding DNA fragment was performed using the pGEX-6P1 vector. Site directed mutagenesis was performed using the QuikChange Lightning Site-Directed mutagenesis kit (Stratagene) and point mutation oligonucleotides (Eurogentec). All constructs and mutations were checked by DNA sequencing (Beckman Coulter Genomics).

Expression of $CSN5_{1\text{-}257}$ wild type (WT) and mutant forms in Rosetta or BL21pLysS *E. coli* cells (Novagen®) and purification were performed using standard conditions. Induced bacterial cells were resuspended in the purification buffer (20 mM Na-2-(N-morpholino)ethanesulfonic acid (Na-MES), pH 6.5, 100 mM NaCl, 0.002% monothioglycerol (MTG)) supplemented with EDTA-free protease inhibitor cocktail (Roche) and were lysed by sonication. Cell lysate was clarified by centrifugation and applied onto a gravity-flow Glutathione Sepharose 4B column (GE Healthcare). Glutathione *S*-transferase (GST)-tagged $CSN5_{1\text{-}257}$ was eluted by 20 mM reduced glutathione in the purification buffer and was cleaved overnight at 4 °C by GST-3C protease. The sample was concentrated and loaded onto a Superdex 75 gel filtration column (GE Healthcare). A final polishing step was used to separate $CSN5_{1\text{-}257}$ from contaminating GST. The resulting pure $CSN5_{1\text{-}257}$ was concentrated to 10 mg mL^{-1} and stored at −80°C until further use. Protein concentrations were measured with a Nanodrop (ThermoScientific) at 280 nm using their theoretical extinction coefficient.

Selenomethionine (SeMet)-labeled $CSN5_{1\text{-}257}$ was expressed in methionine-auxotrophic *E. coli* strain B834 in minimum medium supplemented with SeMet following the manufacturer's instructions (Molecular Dimensions). Although the production yield was smaller, the rest of the purification procedure was unchanged.

The Cullin1/Rbx1 complex was obtained by co-expressing the set of the two ‘split-an-express’ plasmids (pAL-hCul1-NTD, pCool-mRbx1-His-hCul1-CTP) kindly provided by N. Zheng (University of Washington) and distributed by Addgene, following the procedure described in (11). GST-Rbx1/Cul1-CTP/Cul1-NTD was purified from a 0.9 L bacterial culture using a glutathione sepharose column. After thrombin cleavage, the protein solution was subjected to a separation on a Mono S 5/50 column. Fractions corresponding to the Rbx1/Cul1-CTP/Cul1-NTD were pooled, concentrated and stored at -80°C until further use.

Circular dichroism.

Circular dichroism spectra were recorded at 20 °C on a Chirascan spectrophotometer (Applied Photophysics Ltd, UK) equipped with a Peltier thermoregulation system, in 20 mM sodium MES buffer, pH=6.5 with CSN5 protein concentrations of 0.9 mg/ml. The CD spectra for WT and mutant proteins were measured in a cuvette of 0.1-mm path length between 260 nm and 180 nm with a scanning speed of 20 nm/min and a data pitch of 0.5 nm. The data were averaged and corrected for buffer baseline contribution using the Chirascan Pro-Data software. The resulting spectra are presented in Figure S8.

Preparation of Rbx1/Nedd8-Cul1-CTP/Cul1-NTD

420 μg of Rbx1/Cul1-CTP/Cul1-NTD were subjected to neddylation using the Enzo Life Sciences neddylation kit. Neddylation reaction mixture was loaded on a Superdex 75 10/300 GL gel filtration column, equilibrated in 20 mM NaMES pH6.5, 200 mM NaCl, 5 mM DTT, to isolate Rbx1/Nedd8-Cul1-CTP/Cul1-NTD. Rbx1/Nedd8-Cul1-CTP/Cul1-NTD containing fractions were pooled and concentrated to 7 $mg.mL^{-1}$ and stored at -80°C until further use.

Crystallization, data collection and structure determination

Purified $CSN5_{1-257}$ samples were centrifuged through a 0.2-μm filtration unit and subjected to nanolitre crystallization trials using commercial screening kits. Crystals were grown using the sitting drop vapor diffusion method, mixing equal volumes of the protein and the crystallization well solution (0.1 M Na-HEPES, pH 7.5, 27% PEG3350, 0.7 M KSCN). Diffraction data sets were collected on crystals directly frozen in liquid nitrogen. SeMet-labeled CSN5$_{1–257}$ crystals diffracted to 2.6 Å and belonged to the *C*-centered monoclinic space group with two molecules in the asymmetric unit. A dataset was collected at 2.6-Å resolution from a SeMet-labeled CSN5$_{1-257}$ crystal at the ID14-EH4 beamline (ESRF, France) and used to solve the structure using the single-wavelength anomalous dispersion (SAD) method. The dataset was reduced and processed (Table S1) using MOSFLM, SCALA and TRUNCATE from the CCP4 software package (12). The completeness in the last resolution shell fell gradually beyond 2.7 Å due to anisotropic diffraction and radiation-induced damage.

The initial substructure determination and phasing at 2.6-Å resolution performed using AutoSol Wizard of the Phenix package (13) were not successful. Twenty-two heavy-atom sites were localized from anomalous differences data using the charge flipping algorithm (14) as implemented in the SUPERFLIP program (15). All selenium sites except two from SeMet alternate conformations and one zinc site were localized using the SUPERFLIP program (root mean square [r.m.s.] deviation of 0.55 Å with the final refined coordinates). This substructure was used for SAD phasing using the PHASER program (16).

Density modification and automatic tracing in the Resolve program of the Phenix package produced a starting model that assigned 67% of total residues and 48% of side chains. There were two molecules per asymmetric unit as related by a local two-fold axis perpendicular to the crystallographic dyad axis. The structure was completed by iterative model building in Coot (17) and refinement in REFMAC (18) using individual restrained thermal factor refinements and weak non-crystallographic symmetry restraints. The final rounds of refinement were performed using Phenix (13) incorporating six Translation/Libration/Screw (TLS) groups per chain, which produced a model with good statistics and geometry (Table S1) as examined with Molprobity (19). The final model consisted of two chains with residues 2–197 and 219–257, two zinc ions, 52 water molecules, and three thiocyanate ions and was refined to an R_{free} value of 27.4% and an R value of 21.6%. All non-Gly residues fell within the allowed regions of the Ramachandran plot.

Oligomeric state characterization

Protein cross-linking. Purified CSN5$_{1–257}$ solution at 5 mg mL^{-1} was mixed with a six-fold excess of cross-linker dissolved in 20 mM Na-HEPES, pH 7.5, and was incubated on ice between 10 min and 8 h. Four cross-linkers (Pierce) were tested: bis(sulfosuccinimidyl)suberate (BS3), dimethyl suberimidate•2HCl (DMS), 1-ethyl-3-(3-dimethylaminopropyl)carbodiimide hydrochloride (EDC) and ethylene glycolbis(sulfosuccinimidylsuccinate) (sulfo-EGS). The reaction was stopped by adding 50 mM Tris-HCl. Samples were mixed with SDS-PAGE sample loading buffer and separated on a 10% SDS-PAGE gel using Coomassie blue staining to reveal the bands. Expected molecular weights were 29, 58, 87 and 116 kDa for the monomer, dimer, trimer and tetramer, respectively.

Dynamic light scattering experiments. WT and other forms of $CSN5_{1–257}$ and WT $CSN5_{1-252}$ protein samples of 160 μL containing 10 mg mL^{-1} of protein solution were spun for 30 min at 12,000 *g* in a microfuge and measured at 18 °C using a Zetasizer NanoS instrument (Malvern Instruments). From the measured translational diffusion coefficient, the hydrodynamic diameter (D_H) values were calculated using the Stokes-Einstein relation and averaged over three measurements of 13 passes each to ensure accuracy.

Analytical ultracentrifugation. Sedimentation velocity experiments were performed using a Beckman XL-I analytical ultracentrifuge and an AN-50 TI rotor (Beckman Coulter). The experiments were carried out at 20 °C for $CSN5_{1-257}$ WT or L237QL240K variant at 333.0, 167.0, 67.0, 33.0, 17.0 and 3.3 µM in 20 mM NaMES pH 6.5, 100 mM NaCl. A volume of 50 µL (for the four most concentrated samples), 100 µL or 400 µL (for the most diluted one) was loaded into 1.5, 3.0 or 12 mm path cells and centrifuged at 130,000 × g (42,000 rpm). Scans were recorded every 22 min, overnight, by absorbance at 250 and/or 280 nm and by interference. The Sednterp software (freely available at http://www.jphilo.mailway.com/) was used to estimate the partial specific volume of the polypeptide chain, $\bar{v} = 0.734$ mL g^{-1}, the solvent density, $\rho = 1.009$ g mL^{-1}, and the solvent viscosity, $\eta = 1.02$ mPa.s, at 20 °C. Sedimentation profiles were analyzed by the size-distribution analysis of Sedfit. The isotherm of the mean sedimentation coefficients was fitted in term of a monomer-dimer equilibrium constant using the program Sedphat. Sedfit and Sedphat are freely available at http://www.analyticalultracentrifugation.com.

Molecular dynamics simulations.

The A chain from the CSN5$_{1\text{-}257}$ crystal structure was used as the initial structure for MD simulations on the WT protein and the R106 (T, G and P) variants. The missing loop (residues 198–218) was built using the MODELLER program (20, 21). The models of the variants were prepared by mutating the appropriate R106 residue before the solvation step using the Coot software. The atoms within 10 Å of the mutated residue were minimized. All the water molecules from the initial model were removed except the one bound to the catalytic zinc. Rather than using covalent bonds or harmonic restraints to maintain the zinc environment, we employed the cationic dummy atom approach (21), which imposes orientational constraints for the four zinc ligands (His138, His140, Glu151 and water) in the tetrahedral configuration. The protonation state of the other ionisable side chains was set to their normal values at pH 7. The resulting structure was surrounded by a periodic octahedral box of TIP3P water. This procedure resulted in a total of 4,029 protein atoms, including the zinc ion and the catalytic water molecule, solvated by 17,000–18,500 water molecules. All MD simulations were performed with the AMBER11 program (22) with the ff03 force field parameters (23) and the additional force field for the zinc atom environment (21). Optimization and relaxation of solvent were initially performed by means of energy minimizations and MD simulations while keeping the solute atoms constrained to their initial positions with weak force constants.

After equilibration was established by gradually increasing the temperature from 100 to 300 K for 50 ps, the system was subjected to short (100-ps) MD simulations with decreasing constraints at a constant temperature of 300 K and a constant pressure of 1 bar. The 40-ns production run was conducted with constrained bond lengths involving hydrogen atoms and using the Shake algorithm (24), the Verlet integrator with a 2-fs time step for seven the calculation of forces and Langevin dynamics for temperature control. A cut-off radius of 9 Å was used to compute the non-bonded steric interactions. The electrostatic interactions were calculated with the particle-mesh Ewald method (25). The missing counterions were substituted with a net-neutralizing plasma over the periodic box. The ptraj module in the AmberTools package (26) was used to extract data from trajectories and to analyze structural and dynamic properties. All computations including the minimizations and the MD simulations were performed on a HP Z800 workstation equipped with two GPU Tesla C1060 and quad-core Xeon 2.4 GHz processors.

Rotamerically induced perturbations. Large conformational changes, as those frequently coupled to catalytic function, are occurring in the order of 10th of picoseconds to millisecond timescale. Such long computationally demanding MD calculations are thus difficult to simulate. The Rotamerically Induced Perturbation (RIP) method was designed by Ho and Agard (27) to induce large conformational rearrangements of structural segments at the surface of a protein in short simulation times. This new MD approach is particularly useful to identify potentially mobile structural elements or loops. The RIP local thermal excitation of rotameric rotations was applied on each isolated residue in $CSN5_{1-257}$. The kinetic energy transfer to residues in spatial proximity was analyzed to explore the strength of contacts anchoring local segments and reveal their conformational flexibility (28). For each perturbed residue, a 10 ps simulation is produced using the same starting CSN5 monomeric model, equilibrated at 300 K. A RIP perturbation pulse is applied every 100 fs. The MD simulations were performed using the Amber11 package (26) with an GB/SA implicit solvent model and Python scripts implementing the RIP protocol (http://boscoh.com/rip/). The deformability map (average $C\alpha$ r.m.s. deviation values) generated from the analysis of the various trajectories provides an excellent indicator of conformational flexibility and reveals buried tertiary couplings.

Co-immunoprecipitation experiments.

Cell culture medium were from Mediatech Inc (Mannassas, VA) and fetal bovine serum (FBS) were obtained from Gibco (Grand Island, NY). The antibodies used were His-tag (Cell Signaling Technology, Beverly, MA); Flag-tag and β-actin (Sigma-Aldrich, St. Louis, MO). The Lipofectamine Plus and Oligofectamine reagents were from Invitrogen (Carlsbad, CA). Western Lightning Chemiluminescence Plus reagent was from Thermo Scientific Pierce (Rockford, IL). As described in (29), 293T cells were maintained in DMEM supplemented with 10% fetal bovine serum and 100 µg mL^{-1} penicillin and streptomycin. Transfection was carried out using the Lipofectamine Plus reagent (Invitrogen). For the co-immunoprecipitation experiments, cells in the log-phase of growth were collected, washed twice in cold phosphate-buffered saline (PBS), and lysed as described previously (30). Cell lysates were incubated in RIPA buffer for 4 hours at 4 °C with either anti-Flag or anti-His antibodies. Proteins were separated by 12% SDS-PAGE, transferred to nitrocellulose membranes, and probed with anti-His, and anti-Flag antibodies. β-actin was used as the internal positive control for all immunoblots. Immunoreactive bands were detected using HRP-conjugated secondary antibodies with the Western Lightning Chemiluminescence Plus reagent. The protein levels were quantified using ImageJ software (National Institute of Health, Bethesda, MD, USA. http://rsb.info.nih.gov/ij).

Isopeptidase assays using AMC derived substrates.

For the isopeptidase assay using LRGG-AMC substrate, GST-tagged CSN5$_{1\text{-}257}$ protein and different mutants were diluted to 0.2 μg μL^{-1} in reaction buffer (40 mM Tris-HCl pH8.5, 5% glycerol, 1 mM DTT), in the presence of 250 μM LRGG-AMC. The isopeptidase activity of the ubiquitin specific protease 2 catalytic domain (USP2CD; purchased from Boston Biochem.) was used as a control in the same conditions but at a concentration of 0.02 μg μL^{-1}. The effect of zinc chelation was carried out by pre-incubation of CSN5 in the presence of 10 mM ethylene diamine tetraacetic acid (EDTA). The effect of temperature on the isopeptidase activity was evaluated by pre-incubation of the enzymes at 60°C water bath for 20 min. For the isopeptidase assay using Nedd8-AMC substrate, CSN5$_{1\text{-}257}$ protein and different mutants (R106T, R106A, R106G, R106P, E76A, E76A/R106T) prepared in the same conditions were diluted to 0.2 μg μL^{-1} immediately before in the reaction buffer (40 mM Tris-HCl pH8.5, 1 mM DTT). The CSN complex purified from erythrocytes and purchased from Enzo Life Sciences was used at 0.01 μg μL^{-1}. The reactions setup on ice were started by the addition of the substrate (2 μM Nedd8-AMC) to the reaction mixture and followed at 28°C. Isopeptidase assays were monitored in duplicate in a 96-well fluorescence plate on a Tecan Saphire, by following the increase of fluorescence intensity ($\lambda_{excitation}$=380 nm; $\lambda_{emission}$= 460 nm), i.e. the hydrolysis of the isopeptide bond between LRGG/Nedd8 and AMC.

Deneddylation of Rbx1/Nedd8-Cul1-CTP/Cul1-NTD.

The CSN complex at 4.8 ng μL^{-1}, CSN5$_{1\text{-}257}$ protein and R106T variant diluted to 0.33 $\mu g\ \mu L^{-1}$ in 20 mM Tris-HCl pH7.5, 50 mM NaCl were incubated in the presence of 38 μM Rbx1/Nedd8-Cul1-CTP/Cul1-NTD 3 hours at 32°C. Proteins separated on a 10% Tris-tricine gel were transferred on a PVDF membrane and a standard Western blotting protocol was carried out using antibodies specific of Nedd8 (Epitomics) at a dilution of 1:500. Both neddylated cullin 1 and Nedd8 released from the hydrolysis of Nedd8-cullin 1 isopeptide bond were visualized upon chemiluminescence revelation by the SuperSignal West Pico Chemiluminescent Substrate kit (Pierce).

Pull-down experiments.

GST-tagged CSN5$_{1\text{–}257}$ protein (WT and mutant forms) were immobilized on glutathione sepharose 4B beads. His-Nedd8 protein (Boston Biochem.) was added and incubated 20 min on ice prior to extensive washes in 20 mM NaHepes, 150 mM NaCl. Bound proteins were visualized on a precast SDS-Page 4-20% gradient gel (Novus Biologicals) after elution in SDS-Page sample buffer. The gels were stained in Instant Blue dye (Gentaur Molecular Products).

Sequence alignment

The conservation scoring displayed in Fig. 2B and S2 was done by Jalview (31) on the basis of a Clustalw alignment (31) containing the first 173 CSN5 sequences obtained from a human CSN5 BLAST search (32), the first 90 Rpn11 sequences obtained from a human Rpn11 BLAST, the first 76 BRCC36 sequences obtained from a human BRCC36 BLAST search and the first 80 AMSH-LP sequences obtained from a human AMSH-LP BLAST search.

Molecular graphics.

All the structural figures were prepared using PyMOL software (http://www.pymol.org).

Table S1. Data collection and refinement statistics.

PDB code	4F7O
Space group	*C2*
Cell dimensions:	
a, b, c (Å)	161.734, 46.505, 71.261
α, β, γ (°)	90.00, 100.27, 90.00
Resolution (Å)	28.99–2.60
R_{merge}	0.099 (0.367)
$I/\sigma I$	11.6 (3.9)
Completeness (%)	93.4 (68.2)
Redundancy	6.9 (6.6)
Refinement:	
Resolution (Å)	28.99–2.60
No. reflections	15,164 (1573)
$R_{\text{work}}/R_{\text{free}}$	21.6/27.4
No. atoms:	
Protein	3,746
Ligand/ion	9 / 2
Water	52
B-factors:	
Protein	59.5
Ligand/ion	70.1/31.2
Water	43.3
r.m.s. deviations	
Rmsd bond lengths (Å)	0.011
Rmsd bond angles (°)	1.161

Table S2: CSN5 interface surface properties observed in the crystal structure. The total accessible surface area (ASA) and the buried surface area of each protomer are calculated with PISA (1) for each species: dimer A-B generated by local 2-fold symmetry axis (κ=179.7 deg, r.m.s. deviations 0.62 Å on 227 Cα atoms), dimer A-A' generated by crystallographic dyad axis and the D2 tetramer constructed from these two dimers.

	buried and accessible surface area (Å^2)	Number of H-bond contacts	Number of residues implicated in the interfaces	ΔG^{int} (kcal mol^{-1})	ΔG^{diss} (kcal mol^{-1})	Fraction of non-polar buried area (%)
dimer A-B	1,056 12,270	3	34	-14.0	3.6	59
dimer A-A'	975 12,270	11	32	-10.9	2.2	28
tetramer A-A'-B-B'	2,047 12,270	14	66	-51.3	15.8	48

Table S3. Dynamic Light Scattering analyses on CSN5. The average hydrodynamic diameters of the protein (D_H) were calculated from particles size distribution (by volume). The polydispersity index indicates how homogenous the sample appears in the DLS measurement. These values correspond to the average over three measurements. The experiments were performed at 18 °C using 333 μM $CSN5_{1-257}$ solution in 20 mM NaMES pH6.5, 100 mM NaCl.

CSN5 form	**Concentration (μM)**	**Polydispersity index (PDI)**	**Peak intensity (%)**	**D_H (nm)**
1-257 WT	333	0.16	93.2	7.68
1-252 WT	333	0.07	100.0	6.82
1-257 L237Q R129A	333	0.15	97.4	6.22
1-257 L237Q L240E	333	0.12	94.4	6.38
1-257 L237Q L240K	333	0.05	100.0	6.32

Table S4: *c*(*s*) analysis of the sedimentation velocity.

Data are from the profiles acquired at 250 nm for samples at 5 and 10 mg mL^{-1} or 280 nm for more diluted samples. Mean *s*-values were determined in the range 2-6 S. The values for the WT protein and for the L237Q/L240K variant are shown in red and in blue respectively. The sign * denotes a significantly different sedimentation behavior of the sample at the given concentration, with an additional higher sedimentation peak at 7.8S.

CSN5$_{1-257}$ WT/L237QL240K mg mL^{-1} (µM)	Peak 1		Peak 2		Peak 1+2	Aggregates
	s (S)	%	*s* (S)	%	mean *s* (S)	%
10 (333.0)	3.15 3.01	38 90	4.38 4.09	60 10	3.90 3.12	2 5
5 (167.0)	3.09 3.00	48 87	4.23 5.06	45 10	3.64 3.21	7 3
2 (67.0)	3.00 3.06	66 79	3.96 5.29	29 7	3.29 3.24	5 9
1 (33.0)	3.02 2.95	75 77	3.99 4.68	20 8	3.22 3.11	5 10
0.5 (17.0)	3.11 2.91	90 82	N.D. 4.88	N.D. 8	3.11 3.09	10 10
0.1 (3.3)	2.86 N.D.	86 N.D.	4.52 5.04*	7 66*	2.99 5.04	7 12

Table S5: Distances between Zn and ligand atoms in the active site of the CSN5 JAMM motif. The comparison between CSN5$_{1-257}$ crystal structure, MD simulations and Zn-dependant DUB AMSH-LP (PDB entry: 2ZNR; (33)) is presented. The first four ligands belong to the tetrahedral coordination sphere. Residue numbers are indicated in bold for CSN5.

Atom distance (Å)	CSN5$_{1-257}$		AMSH-LP
	x-ray model (A/B)	MD	
Zn NE2 - **H138**/H347	2.07 / 2.10	2.03 ± 0.03	2.04
Zn NE2 - **H140**/H349	2.05 / 2.03	2.05 ± 0.03	2.02
Zn O - **Wat**	2.13 / 2.15	1.86 ± 0.02	1.92
Zn OD2 - **D151**/D360	2.06 / 2.02	2.02 ± 0.03	1.94
Zn CD - **E76**/E292	5.35 / 5.31	5.03 ± 0.25	4.71
Zn OG - **S148**/S357	3.49 / 3.71	3.87 ± 0.30	4.32
Zn CZ - **R106**	5.15 / 4.83	5.13 ± 0.20	-

Figure S1: CSN5 oligomeric state

A. The two types of CSN5 dimers. The dimers with local/crystallographic two-fold symmetry observed in/out of the asymmetric unit are displayed as a surface and ribbon representation. Each monomer is shown in a different color. The monomer surfaces colored in green correspond to the N- and C-terminal extensions outside of the MPN domain. The two-fold axes are displayed.

B. Chemical cross-linking of $CSN5_{1\text{-}257}$ reveals a majority of monomeric and dimeric species and minor higher oligomeric forms in solution. 10% SDS-Page of $CSN5_{1\text{-}257}$ samples (5 mg mL^{-1}) incubated 3 hours on ice in the presence of 1 mM of BS^3 cross linker (1) and (5), EDC (2), DMS (3), sulfo-EGS (4) or none (6). Lanes (1) and (5) correspond to different incubation times (3 and 8 hours). Cross-linking reactions were stopped by the addition of 50 mM Tris-HCl and mixed with SDS-Page loading buffer prior to heat treatment and loading on the electrophoresis gel.

C. Sedimentation velocity experiments of the WT form of $CSN5_{1\text{-}257}$, showing the results of the *c*(*s*) analysis for the protein at 333.0, 167.0, 67.0 and 33.0 μM. The dominant peaks at 3.1 and 4.3 Svedberg units correspond to monomeric and dimeric species, respectively.

D. Fit of the isotherm of sedimentation in the model of a monomer-dimer equilibrium, providing a dissociation constant K_d = 0.7 mM. The confidence interval for K_d is 0.4-1.5 mM considering a 68% confidence level.

E. Sedimentation velocity experiments of the L237QL240K variant form of $CSN5_{1\text{-}257}$, showing the results of the *c*(*s*) analysis for the protein at 333.0, 167.0, 67.0 and 33.0 μM. The dominant peaks at 2.95 and 5.0 Svedberg units correspond to monomeric and, probably, dimeric species, respectively.

F. A–B dimer interface involves the Ins-1 segment. A detailed view of the interfaces maintaining the A–B dimer is shown. Interface residues are represented in violet. Zinc is represented by a green sphere.

G. CSN5 homodimers are disrupted by the LL/QK and R/A mutations. 293T cells were transfected with the CSN5 LL/QK mutation, R/A mutation, or wild type CSN5 for 48 hours and cell lysates were IP with an anti-Flag antibodies and IB with and anti-His antibodies. Cell lysates immunoblotted are shown in the bottom panel. Signal intensities were quantified using ImageJ software.

Figure S2: Structure-based sequence alignment. CSN5 and AMSH-LP sequence alignment on the basis of their respective crystal structures (PDB code for AMSH-LP: 2ZNR) are presented in this figure. Additional information is reported and coded as described hereafter. Secondary structure elements are shown underneath, in red cylinders for α-helices and in blue arrows for β-strands. Strictly conserved residues in the two proteins are noted by a * sign. Residues of the N- and C-terminal extensions present in CSN5 are boxed in green. The 97-131 region (also corresponding to the Ins-1 insertion, as described in the AMSH-LP structure) is found in the two proteins and is highlighted by an orange box. This region adopting different conformations on the two proteins is consequently poorly aligned in the figure. The insertion described in AMSH-LP as Ins-2 (boxed in yellow) that carries a second binding site (zinc binding site motif in AMSH-LP: HPH) is totally disordered in $\text{CSN5}_{1\text{-}257}$ crystal structure, as indicated by […]. Residues that are implicated in CSN5 dimer interface A-B (present in the asymmetric unit) are shown in black and bold (underlined when implicated in a hydrogen bond); those implicated in CSN5 dimer interface A-A’ are shown in blue and bold (underlined when implicated in a hydrogen bond). AMSH-LP residues that are mediating proximal ubiquitin recognition are in green and bold; those responsible for distal ubiquitin recognition are in green, bold and underlined. The conservation of the residues across the species displayed below the alignment are illustrated by color code ranging from red to strictly conserved to light grey for residues that are variable. The conservation scoring was done by Jalview (34) on the basis of a CLUSTALW alignment (35) containing the first 173 CSN5 sequences obtained from a human CSN5 BLAST (32) search.

Figure S3: Conservation of the MPN domain core. Pairwise structural superimposition of CSN5 (in light brown) and a MPN-protein family member (AMSH-LP (pink; PDB code: 2ZNR); CSN6 (yellow; PDB code: 4E0Q), Mov34 (cyan; PDB code: 2O95), Prp8p (magenta; PDB code: 2OG4), AfJAMM (green; PDB code: 1OI0) and SRU-2040 (purple; PDB code: 2KCQ) is presented. N- and C-terminal extensions to the conserved MPN core domain of $CSN5_{1\text{-}257}$ and of Prp8p are shown in light grey.

Figure S4: The MPN domain

A. R.m.s. deviations from the minimized crystal structure of the $CSN5_{1\text{-}257}$ protein during the 40 ns MD simulations. The upper line corresponds to all residues and the lower line to the core residues (residues 25-195; 215-248) excluding N- and C-terminal ends and Ins-2 segment.

B. Fluctuations of $CSN5_{1\text{-}257}$ in the WT and Ins-1 variant forms during MD simulations. Cα atom r.m.s. fluctuations of monomeric CSN5 as a function of residue number during the 40-ns MD simulations are shown for the WT (black), the R106T (blue), the R106G (red) and the R106P (green) forms. Large fluctuations in the 190-220 correspond to the Ins-2 region that is disordered in the crystal structure and that has been modeled for the MD simulations.

C. CSN5 251–255 segment mimics the isopeptidic substrate. Detailed stereo view of the active site shows that in CSN5 (light brown for monomer A; cyan for monomer A' C-terminal region) the Ser254 hydroxyl group occupies a similar position as the AMSH-LP K63-Ub2 isopeptide bond Gly76 carbonyl group (dark grey).

D. Fluctuations of $CSN5_{1\text{-}257}$ zinc binding site during MD simulations. Time dependence of the distance between the catalytic zinc, the side chains of the active site (His138, His140, Asp151, Ser148, Arg106, Glu76) and water molecule during the MD simulations.

Figure S5: *In silico* simulations to explore the flexibility of CSN5.

A. Movements of the Ins-1 region probed by MD simulations. The active site of CSN5 from the crystal structure (light brown ribbon) and from the final snapshot of 40 ns MD simulations (white) is shown. The catalytic residues and those that coordinate the zinc are shown in ball-and-stick representation.

B. The RIP deformability map of monomeric CSN5$_{1\text{-}257}$. RIP perturbations of residues Arg106, Trp136 and Gln155 induce large responses in the Ins-1 region of CSN5$_{1\text{-}257}$ as indicated by the long vertical continuous segments (red). They reveal an inducible marked conformational flexibility of Ins-1 and buried tertiary couplings. In contrast, the intrinsically mobile Ins-2 loop and C-terminal segment (residues 250-257) display significant fluctuations independently of the location of the applied RIP perturbation. The N- and C-terminal CSN5-specific extension are labeled AD-1 and AD-2, respectively. The intensity (red scale) represents Cα r.m.s. deviation above background at the end of each 10 ps simulation.

C. Movements of the Ins-1 region of the R106T CSN5 variant probed by MD simulations. The active site of CSN5 from the crystal structure (light brown ribbon) and from the final snapshot of 40 ns MD simulations (pink) for the R106T variant is shown. The catalytic residues and those that coordinate the zinc are shown in ball-and-stick representation.

Figure S6: Isopeptidase activity of CSN5 on LRGG-AMC hydrolysis. The substrate used in this assay, LRGG-AMC, corresponds to the last four common residues to Nedd8 and ubiquitin, coupled to AMC. The substrate (250 μM) was mixed with CSN5 (WT or R106T) or USP2CD, with or without prior heat or EDTA treatment, and incubated for 10 min at 25°C. The activity was measured by the increase of fluorescence intensity at 460 nm ($\lambda_{\text{excitation}}$ = 380 nm). It is noteworthy that EDTA was used, because ortho-phenanthroline is interfering with the assay.

Figure S7: The R106T form of CSN5 is able to recruit Nedd8. GST-CSN5 (WT or R106T) immobilized on glutathione sepharose beads was incubated in the presence of His-Nedd8 for 20 min on ice. Bound proteins were visualized on a SDS-Page 4-20% gradient SDS-Page after elution in sample buffer. Quantification of the band corresponding to Nedd8, using the

ImageJ software, indicates that Nedd8 binds 4 times more to the R106T variant than the WT form.

Figure S8: Circular dichroism spectra of CSN5 1-257 WT (black line) and of the R106T (blue line), E76A/R106T (green line), R106P (red line) variants.

References.

1. Krissinel E & Henrick K (2007) Inference of macromolecular assemblies from crystalline state. *J Mol Biol* 372(3):774-797.
2. Sharon M*, et al.* (2009) Symmetrical modularity of the COP9 signalosome complex suggests its multifunctionality. *Structure* 17(1):31-40.
3. Fang L*, et al.* (2008) Characterization of the human COP9 signalosome complex using affinity purification and mass spectrometry. *J Proteome Res* 7(11):4914-4925.
4. Fukumoto A, Tomoda K, Kubota M, Kato JY, & Yoneda-Kato N (2005) Small Jab1-containing subcomplex is regulated in an anchorage- and cell cycle-dependent manner, which is abrogated by ras transformation. *FEBS Lett* 579(5):1047-1054.
5. Oron E*, et al.* (2002) COP9 signalosome subunits 4 and 5 regulate multiple pleiotropic pathways in Drosophila melanogaster. *Development* 129(19):4399-4409.
6. Tomoda K*, et al.* (2002) The cytoplasmic shuttling and subsequent degradation of p27Kip1 mediated by Jab1/CSN5 and the COP9 signalosome complex. *J Biol Chem* 277(3):2302-2310.
7. Tomoda K, Yoneda-Kato N, Fukumoto A, Yamanaka S, & Kato JY (2004) Multiple functions of Jab1 are required for early embryonic development and growth potential in mice. *J Biol Chem* 279(41):43013-43018.
8. Holm L & Rosenstrom P (2010) Dali server: conservation mapping in 3D. *Nucleic Acids Res* 38(Web Server issue):W545-549.
9. Pettersen EF*, et al.* (2004) UCSF Chimera--a visualization system for exploratory research and analysis. *J Comput Chem* 25(13):1605-1612.
10. Zhang H, Gao, Z.-Q., Wang, W.-J., Liu, G.F., Shtykova, E.V., Xu, J.-.H., Li, L.-F., Su, X.-D., Dong, Y.-H. (2012) The crystal structure of the MPN domain from the COP9 signalosome subunit CSN6. *FEBS Letters* 586(8):1147-1153.
11. Li T, Pavletich NP, Schulman BA, & Zheng N (2005) High-level expression and purification of recombinant SCF ubiquitin ligases. *Methods Enzymol* 398:125-142.
12. Winn MD*, et al.* (2011) Overview of the CCP4 suite and current developments. *Acta Crystallogr D Biol Crystallogr* 67(Pt 4):235-242.
13. Adams PD*, et al.* (2010) PHENIX: a comprehensive Python-based system for macromolecular structure solution. *Acta Crystallogr D Biol Crystallogr* 66(Pt 2):213-221.
14. Palatinus L, Chapuis, G. (2007) SUPERFLIP - a computer program for the solution of crystal structures by charge flipping in arbitrary dimensions. *J. Appl. Cryst.* 40:786-790.
15. Dumas C & van der Lee A (2008) Macromolecular structure solution by charge flipping. *Acta Crystallogr D Biol Crystallogr* D64(Pt 8):864-873.
16. McCoy AJ*, et al.* (2007) Phaser crystallographic software. *J Appl Crystallogr* 40(Pt 4):658-674.
17. Emsley P & Cowtan K (2004) Coot: model-building tools for molecular graphics. *Acta Crystallogr D Biol Crystallogr* 60(Pt 12 Pt 1):2126-2132.

18. Murshudov GN, *et al.* (2011) REFMAC5 for the refinement of macromolecular crystal structures. *Acta Crystallogr D Biol Crystallogr* 67(Pt 4):355-367.
19. Chen VB, *et al.* (2010) MolProbity: all-atom structure validation for macromolecular crystallography. *Acta Crystallogr D Biol Crystallogr* 66(Pt 1):12-21.
20. Fiser A, Do RK, & Sali A (2000) Modeling of loops in protein structures. *Protein Sci* 9(9):1753-1773.
21. Pang YP, Xu K, Yazal JE, & Prendergas FG (2000) Successful molecular dynamics simulation of the zinc-bound farnesyltransferase using the cationic dummy atom approach. *Protein Sci* 9(10):1857-1865.
22. Case DA (2011) AMBER 11.
23. Duan Y, *et al.* (2003) A point-charge force field for molecular mechanics simulations of proteins based on condensed-phase quantum mechanical calculations. *J Comput Chem* 24(16):1999-2012.
24. Bart E, Kuczera, K., Leimkuhler, B., Skeel, R. (1995) Algorithms for constrained molecular dynamics. *J. Comput. Chem* 16:1192-1209.
25. Essmann U, Perera, L., Berkowitz, M.L., Darden, T., Lee, H., Pedersen, L.G. (1995) A smooth particle mesh Ewald method. *J. Chem. Phys* 103:8577-8593.
26. Case DA, *et al.* (2005) The Amber biomolecular simulation programs. *J Comput Chem* 26(16):1668-1688.
27. Ho BK & Agard DA (2009) Probing the flexibility of large conformational changes in protein structures through local perturbations. *PLoS Comput Biol* 5(4):e1000343.
28. Ho BK & Agard DA (2010) Conserved tertiary couplings stabilize elements in the PDZ fold, leading to characteristic patterns of domain conformational flexibility. *Protein Sci* 19(3):398-411.
29. Kouvaraki MA, *et al.* (2006) Potential role of Jun activation domain-binding protein 1 as a negative regulator of p27kip1 in pancreatic adenocarcinoma. *Cancer Res* 66(17):8581-8589.
30. Pan Y, *et al.* (2012) Jab1/CSN5 negatively regulates p27 and plays a role in the pathogenesis of nasopharyngeal carcinoma. *Cancer Res* 72(7):1890-1900.
31. Thompson JD, Gibson TJ, & Higgins DG (2002) Multiple sequence alignment using ClustalW and ClustalX. *Curr Protoc Bioinformatics* Chapter 2:Unit 2 3.
32. Altschul SF, Gish W, Miller W, Myers EW, & Lipman DJ (1990) Basic local alignment search tool. *J Mol Biol* 215(3):403-410.
33. Sato Y, *et al.* (2008) Structural basis for specific cleavage of Lys 63-linked polyubiquitin chains. *Nature* 455(7211):358-362.
34. Waterhouse AM, Procter JB, Martin DM, Clamp M, & Barton GJ (2009) Jalview Version 2--a multiple sequence alignment editor and analysis workbench. *Bioinformatics* 25(9):1189-1191.
35. Larkin MA, *et al.* (2007) Clustal W and Clustal X version 2.0. *Bioinformatics* 23(21):2947-2948.

Fig. S1

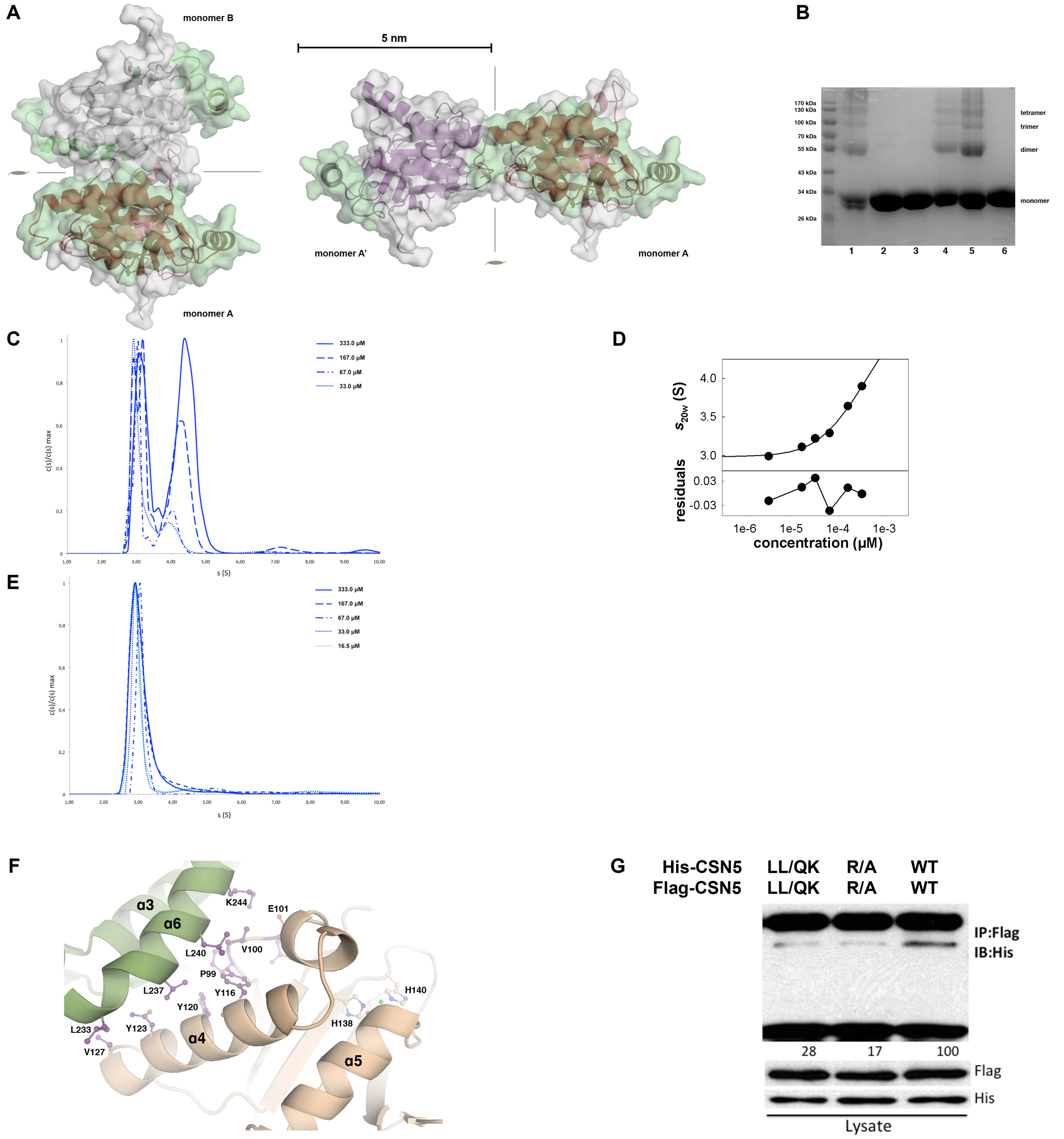
A
monomer B
monomer A
5 nm
monomer A'
monomer A
B
170 kDa
130 kDa
100 kDa
70 kDa
55 kDa
43 kDa
34 kDa
26 kDa
tetramer
trimer
dimer
monomer
1
2
3
4
5
6
C
333.0 µM
167.0 µM
67.0 µM
33.0 µM
c(s)/c(s) max
s (S)
D
s20w (S)
4.0
3.5
3.0
residuals
0.03
-0.03
1e-6
1e-5
1e-4
1e-3
concentration (µM)
E
333.0 µM
167.0 µM
67.0 µM
33.0 µM
16.5 µM
c(s)/c(s) max
s (S)
F
α3
α6
K244
E101
L240
V100
P99
L237
Y116
Y120
H140
L233
Y123
H138
α4
V127
α5
G
His-CSN5
Flag-CSN5
LL/QK
LL/QK
R/A
R/A
WT
WT
IP:Flag
IB:His
28
17
100
Flag
His
Lysate

Fig. S2

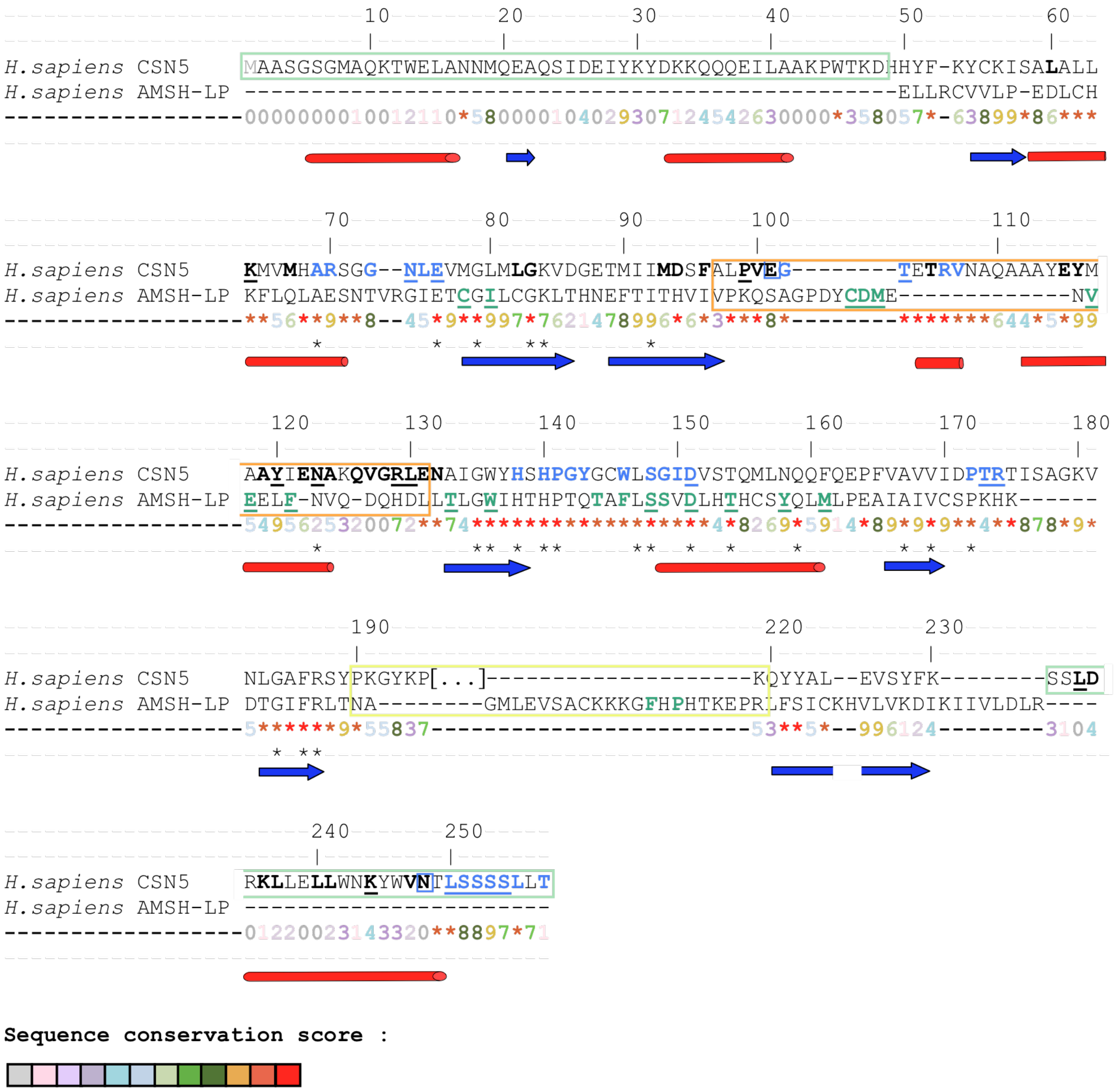
10 20 30 40 50 60
H.sapiens CSN5 MAASGSGMAQKTWELANNMQEAQSIDEIYKYDKKQQQEILAAKPWTKDHHYF-KYCKISALALL
H.sapiens AMSH-LP ---ELLRCVVLP-EDLCH
0000000010012110*5800001040293071245426300000*358057*-63899*86***
70 80 90 100 110
H.sapiens CSN5 KMVMHARSGG--NLEVMGLMLGKVDGETMIIMDSFALPVEG--------TETRVNAQAAAYEYM
H.sapiens AMSH-LP KFLQLAESNTVRGIETCGILCGKLTHNEFTITHVIVPKQSAGPDYCDME------------NV
569**8--45*9**997*7621478996*6*3***8*--------*******644*5*99
120 130 140 150 160 170 180
H.sapiens CSN5 AAYIENAKQVGRLENAIGWYHSHPGYGCWLSGIDVSTQMLNQQFQEPFVAVVIDPTRTISAGKV
H.sapiens AMSH-LP EELF-NVQ-DQHDLLTLGWIHTHPTQTAFLSSVDLHTHCSYQLMLPEAIAIVCSPKHK------
5495625320072**74****************4*8269*5914*89*9*9**4**878*9*
190 220 230
H.sapiens CSN5 NLGAFRSYPKGYKP[...]-------------------KQYYAL--EVSYFK--------SSLD
H.sapiens AMSH-LP DTGIFRLTNA--------GMLEVSACKKKGFHPHTKEPRLFSICKHVLVKDIKIIVLDLR----
5******9*55837-------------------------53**5*--996124---------3104
240 250
H.sapiens CSN5 RKLLELLWNKYWVNTLSSSSLLT
H.sapiens AMSH-LP -----------------------
01220023143320**8897*71
Sequence conservation score :

Fig. S3

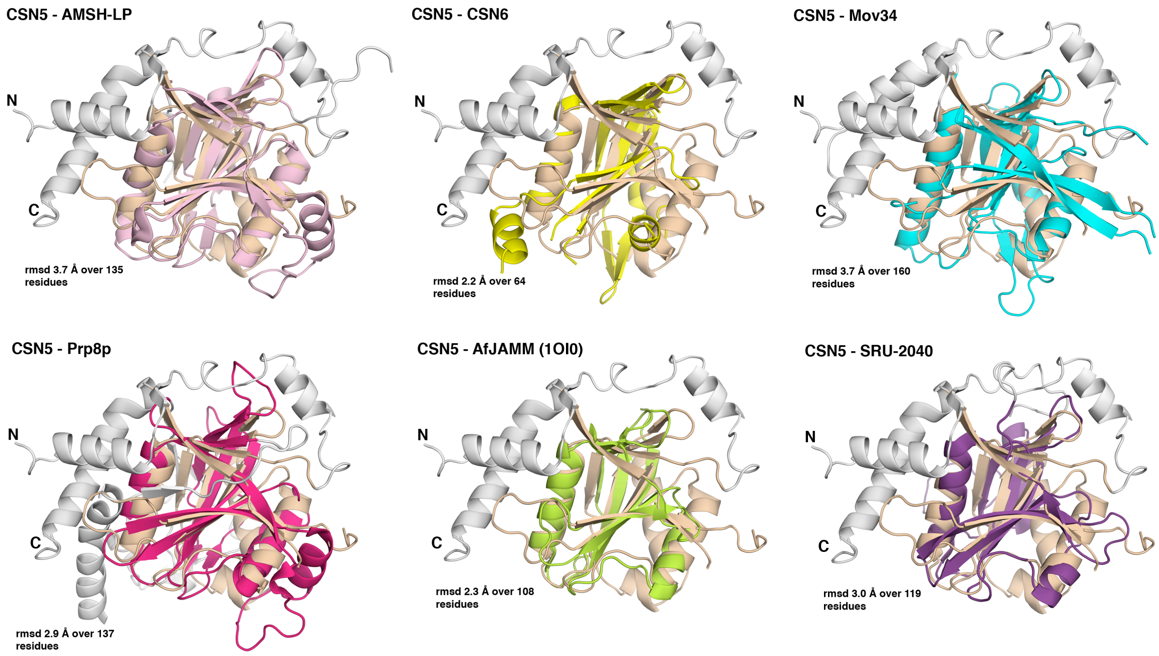
CSN5 - AMSH-LP
N
C
rmsd 3.7 Å over 135 residues
CSN5 - CSN6
N
C
rmsd 2.2 Å over 64 residues
CSN5 - Mov34
N
C
rmsd 3.7 Å over 160 residues
CSN5 - Prp8p
N
C
rmsd 2.9 Å over 137 residues
CSN5 - AfJAMM (1OI0)
N
C
rmsd 2.3 Å over 108 residues
CSN5 - SRU-2040
N
C
rmsd 3.0 Å over 119 residues

Fig. S4

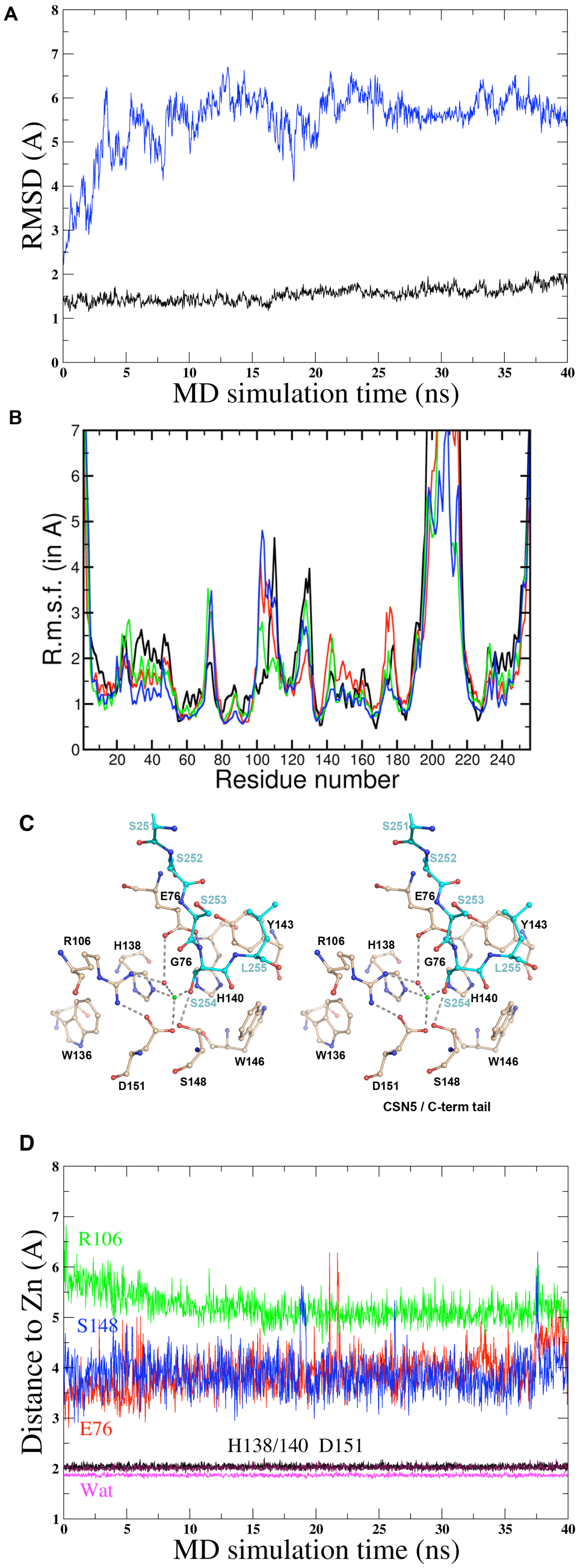

A
RMSD (A)
0
1
2
3
4
5
6
7
8
0
5
10
15
20
25
30
35
40
MD simulation time (ns)
B
R.m.s.f. (in A)
0
1
2
3
4
5
6
7
20
40
60
80
100
120
140
160
180
200
220
240
Residue number
C
S251
S252
E76
S253
Y143
R106
H138
G76
L255
S254
H140
W136
W146
D151
S148
CSN5 / C-term tail
D
Distance to Zn (A)
1
2
3
4
5
6
7
8
R106
S148
E76
H138/140 D151
Wat
0
5
10
15
20
25
30
35
40
MD simulation time (ns)

Fig. S5

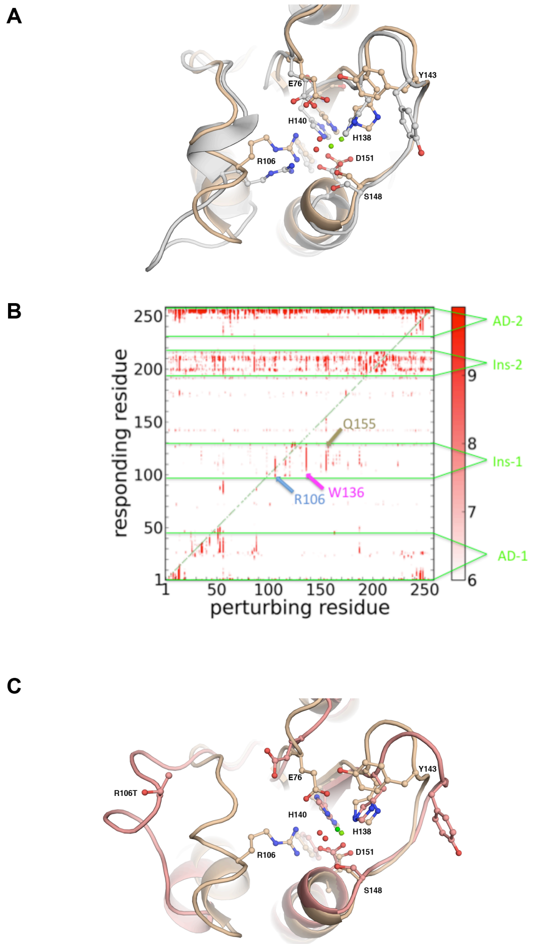
A
E76
Y143
H140
H138
R106
D151
S148
B
250
200
150
100
50
1
responding residue
1
50
100
150
200
250
perturbing residue
Q155
R106
W136
9
8
7
6
AD-2
Ins-2
Ins-1
AD-1
C
R106T
E76
Y143
H140
H138
R106
D151
S148

Fig. S6

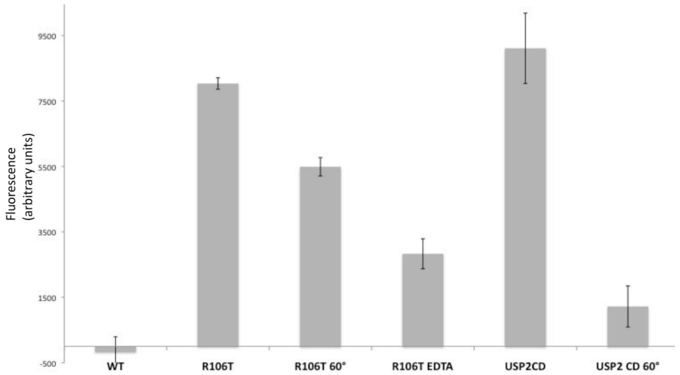
Fluorescence
(arbitrary units)
9500
7500
5500
3500
1500
-500
WT
R106T
R106T 60°
R106T EDTA
USP2CD
USP2 CD 60°

Fig. S7

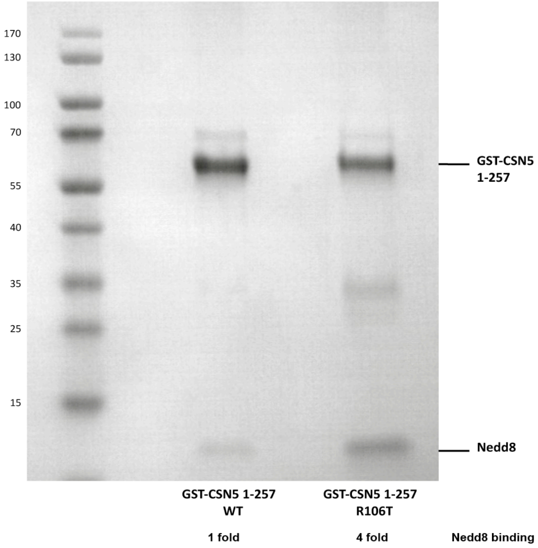
170
130
100
70
55
40
35
25
15
GST-CSN5 1-257
Nedd8
GST-CSN5 1-257 WT
GST-CSN5 1-257 R106T
1 fold
4 fold
Nedd8 binding

Fig. S8

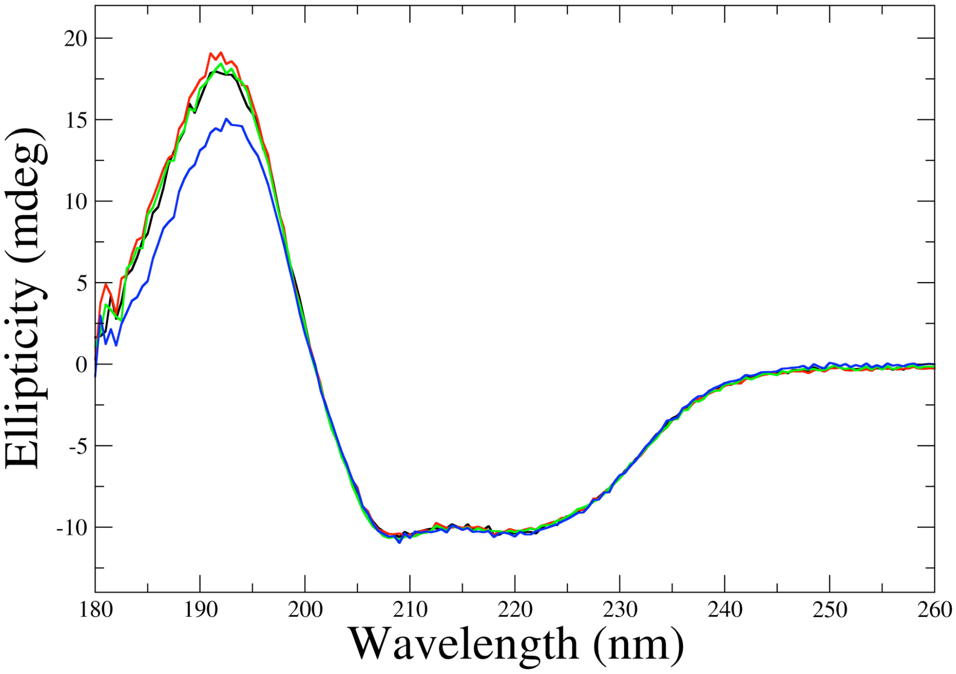
Ellipticity (mdeg)
20
15
10
5
0
-5
-10
180
190
200
210
220
230
240
250
260
Wavelength (nm)